

# Hydride Formation and Decomposition on Cu(111) in HClO<sub>4</sub>

David Raciti\* and Thomas P. Moffat\*



Cite This: *J. Am. Chem. Soc.* 2025, 147, 4038–4051



Read Online

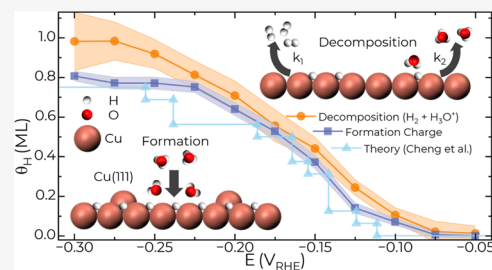
ACCESS |

Metrics & More

Article Recommendations

Supporting Information

**ABSTRACT:** Cu electrodeposition and the electrocatalysis of hydrogenation reactions thereupon involve significant interactions with adsorbed hydrogen. Electrochemical mass spectrometry (EC-MS) is used to explore the formation and decomposition of surface hydride on Cu(111) in 0.1 mol L<sup>-1</sup> HClO<sub>4</sub>. Hydride formation is associated with two reduction waves that reflect the potential-dependent H<sub>ads</sub> coverage and its reconstruction. Voltammetric cycling reveals an additional oxidative and reductive feature at ≈ -0.05 V versus the reversible hydrogen electrode (RHE) that reflects the state of the 2D surface hydride. Extending the voltammetric window to more negative potentials results in an increase in H<sub>ads</sub> coverage and surface reconstruction that subsequently leads to accelerated hydride decomposition at positive potentials. Voltammetric and chronoamperometric analysis of hydride formation indicates a H<sub>ads</sub> coverage of ≈0.75 monolayers (ML) between -0.225 V vs RHE and -0.275 V vs RHE with further increases in H<sub>ads</sub> observed with the onset and acceleration of the HER at more negative potentials. Returning to more positive potentials, hydride decomposition begins above -0.05 V vs RHE. Recombination of H<sub>ads</sub> to form H<sub>2</sub> accounts for desorption of ≈0.5 ML of H<sub>ads</sub> while its oxidation to H<sub>3</sub>O<sup>+</sup> consumes between ≈0.15 and ≈0.4 ML of H<sub>ads</sub>, depending on the specific electrochemical conditions. The potential-dependent H<sub>ads</sub> coverage and surface reconstruction are congruent with trends identified in recent computational and electrochemical scanning tunneling microscopy studies. In contrast to perchloric acid, the presence of strongly adsorbing anions, such as sulfate or halides, favors hydride decomposition via the recombination pathway.



## INTRODUCTION

The technological impact of Cu spans a wide range from its ubiquitous presence in microelectronic interconnects to its use as a catalyst in emergent electrosynthetic reactions relevant to the electrification of the chemical industry.<sup>1–5</sup> In these applications, the interaction of Cu with hydrogen exerts important effects that need to be understood. In electrolytic and electroless Cu deposition, hydrogen can be incorporated within growing films, thereby impacting their physical properties and even stimulating room temperature recrystallization.<sup>6–11</sup> Under more aggressive conditions, cogeneration of hydrogen gas during electrodeposition can be utilized to template the growth of 3-D Cu foams for use in thermal management, bonding, and electrocatalysis.<sup>12</sup> Excursions to such negative potentials can also lead to cathodic corrosion that is likely related to hydride formation.<sup>13</sup>

Of particular interest is the finding that Cu is the only elemental electrocatalyst capable of efficiently reducing CO<sub>2</sub> to hydrocarbons and oxygenates. In a related fashion, Cu–H functionalized molecules have a long history in organic synthesis as potent reaction centers for CO<sub>2</sub> reduction.<sup>14–16</sup> For such multistep hydrogenation reactions, competitive and coadsorption between CO, H, and other reaction intermediates play a central role and likewise are known to induce and guide potential-dependent mesoscale rearrangements of Cu surfaces.<sup>13–15,17–20</sup> The interaction of CO with Cu surfaces has received substantial attention, while the role of adsorbed

hydrogen and its interactions with CO in various hydrogenation reactions remains understudied and unresolved.<sup>21</sup> It is also noteworthy that some years ago UHV studies of hydrogenation reactions on hydrogen-dosed surfaces demonstrated that subsurface hydrogen species can serve as active intermediates although the possibility of such pathways has received limited attention in electrochemical systems.<sup>22–24</sup> Studies of different synthetic pathways for producing bulk crystalline CuH yield different surface properties that speak to the complexity of the system and the need for further study.<sup>25</sup> UHV studies of hydrogen adsorption on low-index Cu surfaces reveal the formation of two-dimensional surface hydride superlattices and also provide the earliest measurement of competitive adsorption dynamics between H and CO albeit at low temperatures.<sup>26–32</sup> More recently, operando methods like electrochemical scanning tunneling microscopy (ECSTM), shell-isolated nanoparticle enhanced Raman spectroscopy (SHINERS), and electrochemical mass spectrometry (EC-MS) have been utilized to study H adsorption on copper surfaces in electrolytic environments.<sup>33–37</sup> A complex, but stoichiometric, (4 × 4) hydride

Received: September 13, 2024

Revised: January 9, 2025

Accepted: January 15, 2025

Published: January 27, 2025



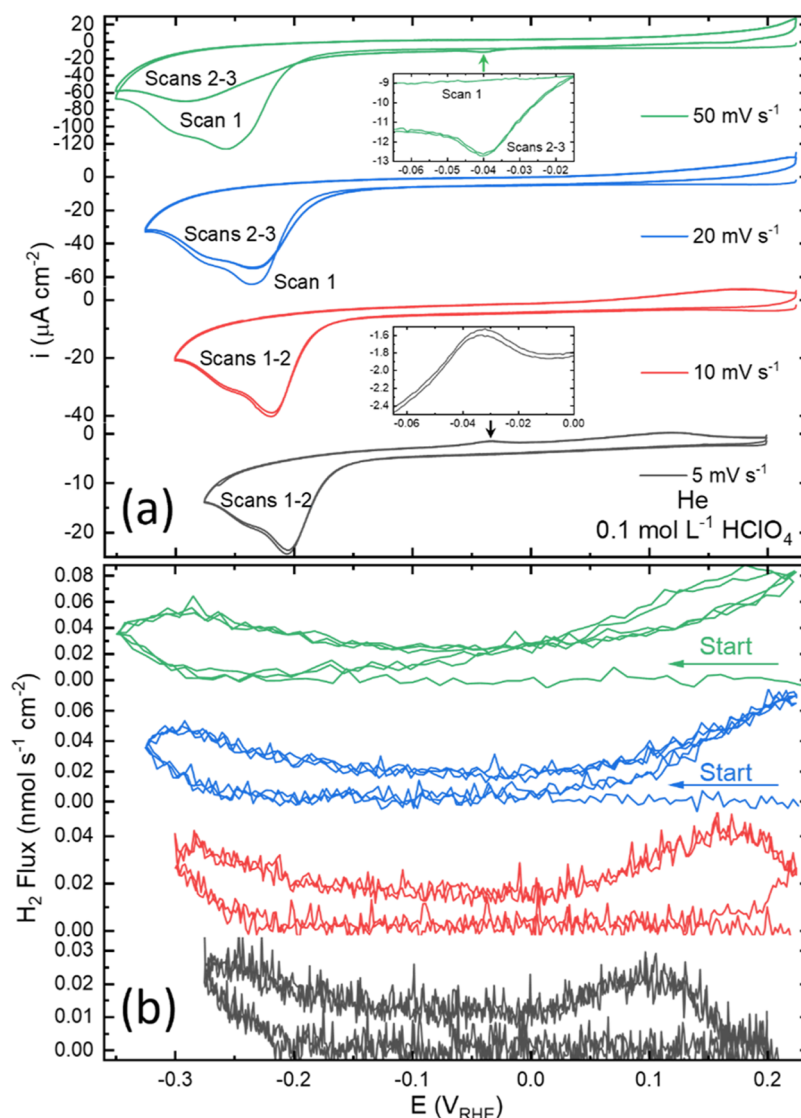


**Figure 1.** (a) Voltammetry and (b) 2 amu  $\text{H}_2$  flux measured at different scan rates in the thin layer EC-MS cell reveal hydride formation and decomposition for Cu(111) in  $0.1 \text{ mol L}^{-1} \text{HClO}_4$ .

overlayer structure was imaged on Cu(111) in sulfuric acid.<sup>33,34</sup> Meanwhile EC-MS measurements indicate a potential regime where a saturated hydride phase is formed with a coverage of  $(0.67 \pm 0.15)$  monolayers (ML) in  $0.1 \text{ mol L}^{-1} \text{H}_2\text{SO}_4$ .<sup>36</sup> Asymmetric voltammetry arises from the slow formation of the hydride phase by proton reduction with development of a  $\approx 1040 \text{ cm}^{-1}$  vibrational band during the negative-going scan. Its subsequent desorption by hydrogen recombination occurs on the positive-going scan that is stimulated by anion adsorption (sulfate band at  $1200 \text{ cm}^{-1}$ ).<sup>35</sup> Recent atomistic simulations indicate that hydrogen-induced reconstruction of Cu(111) creates Cu adatoms that facilitate both the hydrogen evolution reaction (HER) and  $\text{CO}_2/\text{CO}$  reduction in acidic environments subject to competitive interactions in the operational environment.<sup>33,38,39</sup>

In the present study, the formation of surface hydride on Cu(111) in  $0.1 \text{ mol L}^{-1} \text{HClO}_4$  is examined with proton reduction partitioned between hydride formation and HER. Voltammetric EC-MS measurements reveal at least two electrochemical peaks related to surface hydride formation on Cu(111), that involve populating different surface sites and/or

phase transitions and reconstructions, while subsequent hydride decomposition at more positive potentials is associated with a single voltammetric wave. In contrast to studies with sulfate ( $\text{SO}_4^{2-}$ ) or chloride ( $\text{Cl}^-$ ), perchlorate ions ( $\text{ClO}_4^-$ ) are not expected to specifically adsorb on copper surfaces, yet measurable oxidative current is still observed at potentials that overlap with hydride decomposition at higher potentials.<sup>35,40</sup> Chronoamperometric EC-MS measurements were employed to quantify the  $\text{H}_{\text{ads}}$  coverage with particular attention given to partitioning the hydride decomposition between  $\text{H}_{\text{ads}}$  recombination versus electrochemical oxidation back to hydronium.

## EXPERIMENTAL SECTION

**Preparation of the Cu(111) Electrode.** Before EC-MS measurements were conducted, the 5 mm diameter Cu(111) crystal was mechanically polished using an alumina slurry to achieve a  $0.05 \mu\text{m}$  finish. This was followed by rinsing and sonicating the specimen in water multiple times to eliminate any remaining alumina particles. Subsequently, the Cu(111) disk was electropolished for 5 min at  $+1.6 \text{ V}$  vs a Pt counter electrode, in  $85\% \text{H}_3\text{PO}_4$ . The Cu(111) surface was positioned facing upward and opposite of the gas-generating Pt gauze that was  $\approx 6 \text{ cm}$  away. Following  $\approx 10 \text{ min}$  of electropolishing, the disk

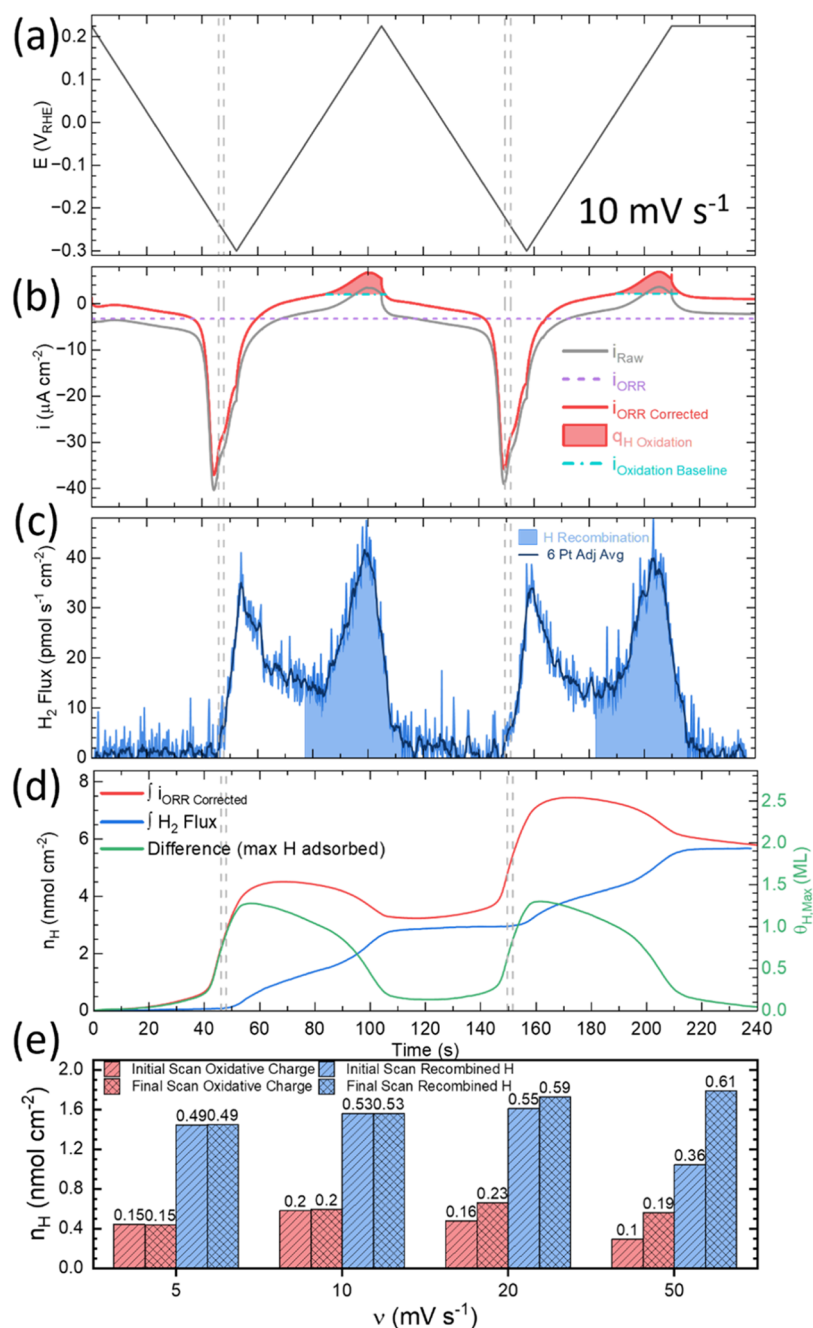


**Figure 2.** Traces of (a) potential, (b) current, and (c)  $H_2$  flux vs time from  $10\text{ mV s}^{-1}$  voltammetry shown in Figure 1. (d) Integration of (b) current and (c)  $H_2$  flux as well as their difference in the form of atomic hydrogen ( $\text{mol cm}^{-2}$ ). (e) Decomposition of the hydride is quantified by the charge associated with oxidation of  $H_{\text{ads}}$  to  $H_3O^+$  (shaded red in (b)) and the amount of  $H_2$  produced by recombination (shaded blue in (c)). The analyses for the initial and final cycle at different scan rates in Figure 1 are summarized (e) with the fractional  $H_{\text{ads}}$  surface coverage indicated on the top of the respective bars. The group of two dashed lines indicates the potential region for onset of HER.

was rinsed and then shielded with  $H_2O$  until being dried with flowing Ar immediately before being mounted in the mass spectrometer.

**Electrochemical Mass Spectrometry Measurements.** EC-MS was performed using a thin layer cell configuration (Spectro Inlets\*).<sup>41,42</sup> Experiments were performed in freshly prepared Ar purged  $0.1\text{ mol L}^{-1}$   $HClO_4$  electrolyte (70%  $HClO_4$ , 99.999% trace metal basis from Sigma-Aldrich). Glass side arms on opposite sides of the working electrode contained an Ir wire counter electrode and a capillary consisting of a Pt wire submerged in  $H_2$  saturated electrolyte to form a trapped  $H_2$  bubble quasi-reversible hydrogen reference electrode (RHE), respectively. The Ir counter electrode was placed  $>3\text{ cm}$  away from the entrance to the working electrode compartment to minimize any contribution from the counter-reactions. To mitigate oxidation and

dissolution of the Cu(111) working electrode that will occur under open circuit conditions, potentiostatic control at  $0\text{ V}$  vs RHE (to be assumed throughout) was imposed immediately following wetting of the three electrodes by the electrolyte. For subsequent rest or idle periods between electrochemical measurements, the working electrode was typically poised at  $0.175\text{ V}$ . A Biologic SP-200 potentiostat was used for all electrochemical measurements. The EC-MS and electrochemical data were collected on the same computer enabling effective time synchronization between the two measurements. For cyclic voltammetry measurements, the baseline of the  $2\text{ amu}$  EC-MS signal was subtracted using a linear profile with the slope determined by averaging the signal over  $2\text{ s}$  before and after completion of the voltammetric scan.

For negative step potential pulse measurements, the 2 amu baseline was zeroed by averaging the signal for  $\approx 2$  s prior to initiating each potential step ( $E_{\text{pulse}}$ ) (Figure S1). The approach is congruent with the absence of steady-state HER occurring at the rest potential of 0.175 V ( $E_{\text{rest}}$ ). For positive step potential pulse measurements, determining the background for the 2 amu  $\text{H}_2$  measurement is more difficult. Fortunately, extended observation of the MS baseline drift indicates that, absent an obvious input source, the baseline for 32 amu ( $\text{O}_2$ ) and 2 amu ( $\text{H}_2$ ) change at the same rate. Accordingly, the 32 amu signal is used to provide an estimate of the drift in the  $\text{H}_2$  background levels. The utility of this alignment is evident in Figure S2 where the drift in the 32 amu signal was used to estimate the baseline signal for 2 amu (red line). It is noteworthy that when  $E_{\text{rest}} > 0$  V, where no HER occurs, the 2 amu signal drops to the baseline, overlapping the 32 amu baseline signal, supporting this strategy.

The 2 amu signal was converted to  $\text{H}_2$  flux following the strategy discussed previously.<sup>36</sup> In short, calibration curves were generated under steady-state HER conditions that use the current, converted to  $\text{H}_2$  flux, to calibrate the 2 amu signal using either Cu or Pt electrodes. The electrolyte thickness separating the working electrode from the membrane entrance to the quadrupole mass spectrometer was determined using impulse measurements discussed previously and was typically found to be  $\approx 120$   $\mu\text{m}$ .<sup>36,43</sup>

Impedance measurements of Cu(111) mounted in the EC-MS were conducted in 0.1 mol  $\text{L}^{-1}$   $\text{HClO}_4$  using a 10 mV perturbation with a range of 100 mHz to 100 kHz using 10 points per decade. Measurements were performed as the potential was advanced from 0.2 to  $-0.25$  V in 50 mV increments. The Nyquist plots (Figure S3) were fit to a simplified Randle circuit, and the results are presented in Table S1.

## RESULTS AND DISCUSSION

### Cyclic Voltammetry on Cu(111) in 0.1 mol $\text{L}^{-1}$ $\text{HClO}_4$

Recent EC-MS studies have revealed the formation of surface hydride on Cu(111) in various acid electrolytes.<sup>35</sup> For 0.1 mol  $\text{L}^{-1}$   $\text{HClO}_4$ , hydride formation is associated with two overlapping voltammetric reduction peaks, e.g., at  $-0.22$  and  $-0.26$  V for 10  $\text{mV s}^{-1}$ , in Figure 1a while only a single peak is observed in electrolytes containing  $\text{SO}_4^{2-}$ ,  $\text{Cl}^-$  and  $\text{PO}_4^{3-}$ . The origin of the two voltammetric peaks in perchloric acid is unresolved although recent theoretical work on H adsorption on Cu(111) indicates a series of phase transitions with increasing H coverage.<sup>33,38</sup> For a pH of 1, an equilibrium H coverage of 0.56 ML is predicted between  $-0.200$  and  $-0.241$  V followed by an increase in coverage to 0.75 ML between  $-0.250$  and  $-0.426$  V coincident with the development of  $(4 \times 4)$  superlattice seen in EC-STM experiments.<sup>34,40</sup> At more negative potentials, surface reconstruction occurs with the formation of an ordered  $(4 \times 4)$  array of Cu adatoms stabilized by the higher H coverages  $> 0.94$  ML. It should be noted that the computational uncertainties with the DFT exchange correlation functional, and the solvation and electrolyte models are such that the stated potentials could be off by up to  $\pm 0.3$  V.<sup>33</sup>

Variation of the scan rate from 5 to 50  $\text{mV s}^{-1}$  induces a  $\approx -50$  mV shift in the reduction wave peak potentials indicative of a kinetic constraint on surface hydride formation (Figure 1). This shift is not due to ohmic losses, as EIS measurements reveal the solution resistance to be  $20.6 \pm 0.6$  Ohms (see Figure S3 and Table S1), which would result in  $< 1$  mV shift in the peak potential for the peak current measured in the 50  $\text{mV/s}$  scan. Continued voltammetric scanning at rates  $\geq 20$   $\text{mV s}^{-1}$  reveals that hydride decomposition is not completed during the first cycle, and as a result, the peak proton reduction current to reform the hydride during subsequent cycles is noticeably diminished (Figure 1a). Additionally, a small reduction peak develops near  $-0.05$  V, which is associated with the incomplete

removal of the hydride phase during the first voltammetric cycle. The magnitude of the peak at  $-0.05$  V increases with scan rate, when cycling without interruption, as shown in Figure S4. During the return scan to positive potentials, the EC-MS reveals evolution of  $\text{H}_2$  at potentials above 0.0 V due to the decomposition of the hydride phase by  $\text{H}_{\text{ads}}$  recombination (Figure 1b) with the onset and rate of the decomposition being sensitive to the presence of anions and more specifically their strength of adsorption.<sup>35</sup> Strongly adsorbing  $\text{Cl}^-$  shifts hydride decomposition to potentials negative of 0.0 V, Figure S5, while the much weaker interaction with  $\text{ClO}_4^-$  is such that the  $\text{H}_{\text{ads}}$  combination process is still underway at the upper vertex at 0.2 V. The final increments of  $\text{H}_{\text{ads}}$  do not leave the surface until the second negative-going scan as evidenced by the measured  $\text{H}_2$  flux (Figure 1b), better visualized when plotted vs time (Figure 2). For faster scan rates, even less decomposition of hydride occurs by the end of the first cycle (Figures 1b, S6, and S7). Detection of  $\text{H}_2$  from recombination is apparent at potentials  $> -0.05$  V (Figure 1b) with the final increments that are detected on the negative scan reflecting the slow kinetics of decomposition and diffusional lag in  $\text{H}_2$  collection.

An alternative pathway to hydride decomposition by recombination is oxidation to  $\text{H}_3\text{O}^+$ . As an upper bound the measured anodic charge, denoted  $q_{\text{H Oxidation}}$ , of  $(48 \pm 14)$   $\mu\text{C cm}^{-2}$  for this process corresponds on average to removal  $\Delta\theta_{\text{H}}$  of  $(0.17 \pm 0.05)$  ML of  $\text{H}_{\text{ads}}$  (Figure 2b,e) following eq 1,

$$\Delta\theta_{\text{H}} = \frac{n_{\text{H}^+}}{\rho_{\text{Cu}(111)}} = \frac{q}{zF\rho_{\text{Cu}(111)}} \quad (1)$$

where  $q$  is the charge density ( $\text{C/cm}^2$ ),  $z$  is the number of electrons transferred ( $\text{mol e}^-/\text{mol H}$ ),  $F$  is Faraday's constant ( $\text{C/mol e}^-$ ),  $n_{\text{H}^+}$  is the moles of  $\text{H}^+$  produced ( $\text{mol H/cm}^2$ ), and  $\rho_{\text{Cu}(111)}$  is the atomic surface density of Cu(111) which is 2.935  $\text{nmol/cm}^2$ .

The possibility that  $\text{H}_{\text{ads}}$  displacement by recombination to  $\text{H}_2$  is driven by the adsorption of trace anion contaminants was evaluated. The most likely contaminants are  $\text{Cl}^-$  and  $\text{PO}_4^{3-}$  with the former being an impurity in the as-received perchloric acid and the latter being carried over from electropolishing. Voltammetry, at 5  $\text{mV s}^{-1}$  following titration of 0.1 mol  $\text{L}^{-1}$   $\text{HClO}_4$  with 100  $\mu\text{mol L}^{-1}$   $\text{HCl}$ , reveals that  $\text{Cl}^-$  adsorption drives decomposition of the hydride phase by  $\text{H}_{\text{ads}}$  recombination, which peaks at  $-0.08$  V before reaching completion below 0 V (Figure S5a). Halide addition also shifts hydride formation to more negative potentials, with the peak current only being reached near  $-0.3$  V as the adsorbed  $\text{Cl}^-$  must desorb before the hydride can form. For a more dilute  $\text{Cl}^-$  concentration of 10  $\mu\text{mol L}^{-1}$  (Figure S5b), halide adsorption and hydride decomposition shift to more positive potentials. Both the current and EC-MS peaks split into two broad but distinguishable events. The first is centered near  $-50$  mV with the second near  $+75$  mV with the peak separation reflecting the mixed control kinetics associated with the transport-limited halide flux relative to the scan rate. In contrast,  $\text{Cl}^-$  desorption and hydride formation on the negative-going scan appear as a single wave, indicating a saturated halide surface coverage is already present at this point in the experiment. The hydride formation peak shifts slightly positive to  $-0.275$  V consistent with thermodynamic expectations for  $\text{Cl}^-$  desorption at the more dilute concentration. Finally, for the 1  $\mu\text{mol L}^{-1}$   $\text{Cl}^-$  titration both the voltammetry and EC-MS  $\text{H}_2$  flux profile (Figure S5c) are similar to that in neat 0.1 mol  $\text{L}^{-1}$   $\text{HClO}_4$  although some differences

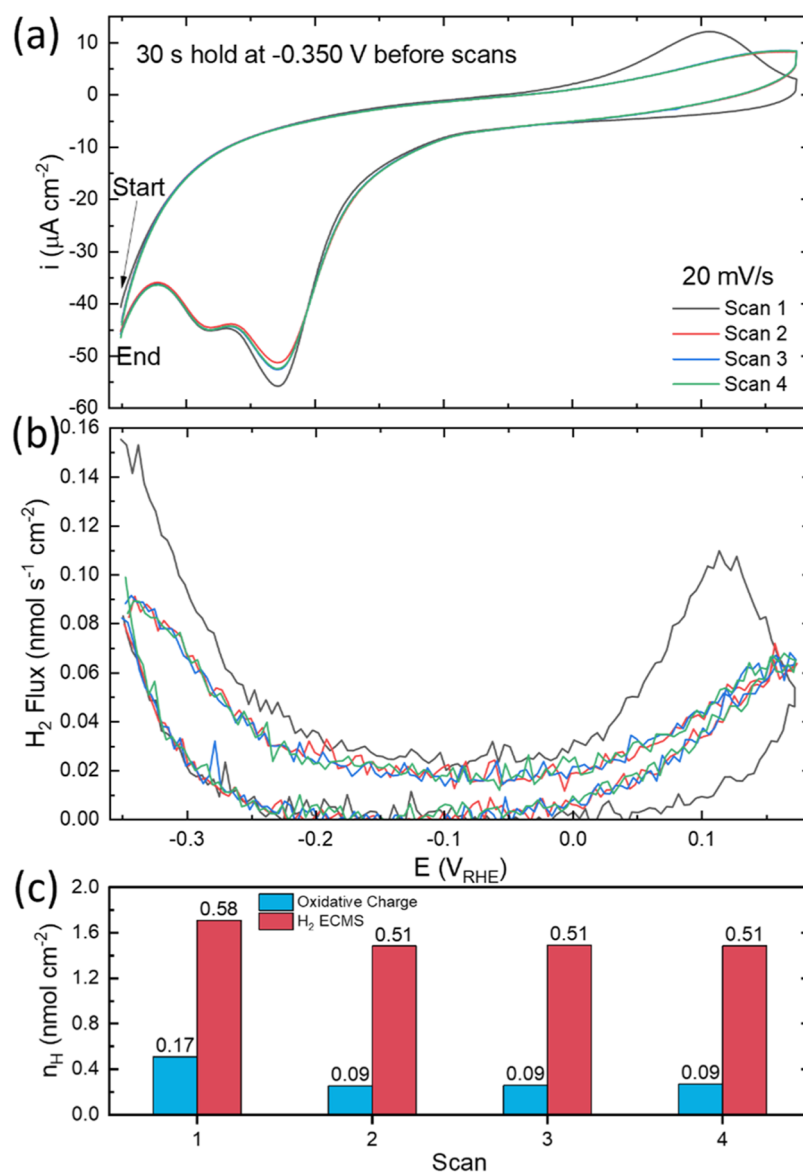


**Figure 3.** (a) Cyclic voltammetry of Cu(111) in He-saturated 0.1 mol L<sup>-1</sup> HClO<sub>4</sub> and the accompanying (b) H<sub>2</sub> flux measured by EC-MS following an initial 30 s pretreatment at -0.350 V. The H<sub>2</sub> flux and oxidative peak at the anodic sweep were (c) integrated and converted to n<sub>H</sub> (nmol cm<sup>-2</sup>) and are labeled above the bar graph in terms of the H<sub>ads</sub> fractional surface coverage θ<sub>H</sub>.

remain. During the positive sweep the onset of Cl<sup>-</sup> adsorption between -50 and -25 mV is followed by mass transport-limited accumulation which displaces the hydride at a fixed rate of ≈ 0.15 nmol s<sup>-1</sup> cm<sup>-2</sup> that is sustained to the upper potential limit. In contrast, in Cl<sup>-</sup> free solution (Figure 1a), the primary anodic wave and hydride decomposition peak at 5 mV s<sup>-1</sup> occur at a much more positive potential near +0.1 V. A small oxidative adsorption wave is evident near ≈ -0.04 V that reflects some change in the hydride phase prior to the onset of its decomposition. Interestingly, a similar peak develops in Cl<sup>-</sup> containing media that was ascribed to a phase transition in the Cl<sup>-</sup> adlayer however in that experiment the feature only appears after multiple voltammetric cycles.<sup>44,45</sup> Further work will be required to understand the nature of this small feature.

Integration of the voltammetric current and H<sub>2</sub> flux, following baseline subtraction and conversion of the 2 amu signal (see the Experimental Section), provides an avenue to track H coverage with time and assess the total collection ability of the thin layer EC-MS cell as summarized in Figure 2. Care must be taken in

evaluating the baseline and contributions from possible background reactions, such as residual O<sub>2</sub> reduction. For fast scan rates and low Faradaic currents, the electrode charging capacitance is significant but largely nulled by integration over each complete voltammetric cycle. At slower scan rates, the parasitic current due to transport-limited reduction of residual O<sub>2</sub> is evident in the background offset of the voltammetric current. For scan rates <10 mV/s this is compensated by subtracting a fixed current offset as indicated in Figures 2 and S6. Following this correction and considering H<sub>2</sub> and H<sub>3</sub>O<sup>+</sup> as the only reactants involved, the H coverage at a given potential is estimated from the difference of the integrated current and H<sub>2</sub> flux from the EC-MS signal converted to n<sub>H</sub> or θ<sub>H</sub> (using ρ<sub>Cu(111)</sub>) respectively as shown in Figure 2d and summarized in Figure 2e. Implicit cancellation of the pseudocapacitance contribution following a complete voltammetric cycle should lead to closure of the H<sub>ads</sub> coverage vs potential relationship consistent with total EC-MS collection of H<sub>2</sub> generated under these conditions. The slow kinetics of recombination hinder

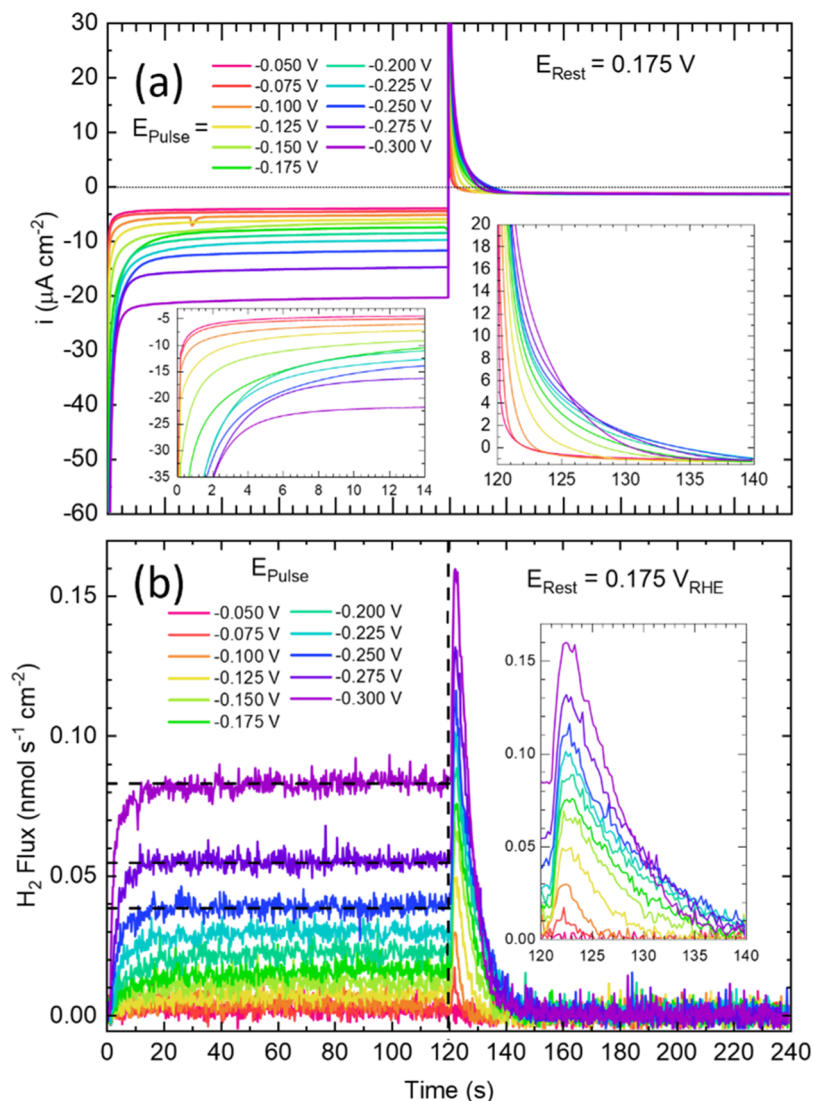


**Figure 4.** (a) Chronoamperometry and (b)  $\text{H}_2$  flux during potential pulse measurements on Cu(111) in He-saturated  $0.1 \text{ mol L}^{-1} \text{ HClO}_4$ . The horizontal dotted line in (a) indicates zero current. The horizontal dashed lines in the  $\text{H}_2$  flux plot indicate the steady-state HER ( $\text{HER}_{\text{ss}}$ ) flux at the three most negative  $E_{\text{pulse}}$  as determined by averaging the last 60 s of the flux during  $E_{\text{pulse}}$ . The vertical dashed line indicates the transition to  $E_{\text{rest}}$ . The insets in (a) magnify the transient components of current for both  $E_{\text{pulse}}$  and  $E_{\text{rest}}$  and the inset in (b) magnifies the transient period at  $E_{\text{rest}}$  associated with the decomposition of hydride to  $\text{H}_2$  via  $\text{H}_{\text{ads}}$  recombination.

such closure for the first voltammetric cycle, although with continuing cycling a closed loop steady-state result is observed in Figure S7.

The proton reduction charge that goes to form  $\text{H}_{\text{ads}}$  prior to MS detection of the onset of  $\text{H}_2$  from the HER, (denoted in Figures 2 and S6 by the two vertical dashed lines) corresponds to a maximum possible  $\text{H}_{\text{ads}}$  coverage of  $(0.82 \pm 0.02)$  ML regardless of scan rate or cycle number. Comparison of estimated hydride coverage at the HER onset potentials of  $-0.226$ ,  $-0.245$ ,  $-0.260$ , and  $-0.290 \text{ V}$  for scan rates of 5, 10, 20 and  $50 \text{ mV s}^{-1}$ , respectively, for different scan rates are summarized in Figures S6–S7 and Table S2. The threshold also aligns with the inflection evident between the two voltammetric current peaks that comprise the reduction wave. The subsequent onset of HER is consistent with a further increase in H coverage that might induce the surface-subsurface H phase transition and/or reconstruction of Cu(111) seen in EC-STM experiments wherein the extracted Cu adatoms serve to coordinate and catalyze the hydrogen evolution reaction.<sup>33,34</sup>

Integrating the  $\text{H}_2$  flux from  $-0.050 \text{ V}$  on the positive voltammetric sweep until the background signal is reached again yields between  $0.6 \text{ nmol cm}^{-2}$  and  $0.9 \text{ nmol cm}^{-2}$  of  $\text{H}_2$ . This corresponds to a conservative estimate of fractional  $\text{H}_{\text{ads}}$  coverage ( $\theta_{\text{H}}$ ) between 0.36 and 0.61 ML (Figure 2e) depending on the scan rate and negative vertex potential. The integrated H coverage measured for the final voltammetric cycle at 20 and  $50 \text{ mV s}^{-1}$  is larger than the preceding scans since the potential was held for an extended period at the upper vertex after the voltammetric sweep was finished while collection of the evolved  $\text{H}_2$  continued. The result is congruent with the incomplete decomposition of the hydride phase seen at higher scan rates due to limited recombination kinetics and insufficient time spent at the decomposition potentials. An upper bound on  $\theta_{\text{H}}$  can be estimated by summing the oxidative and H recombination portions for each respective scan rate seen in Figure 2e. The increase in  $\theta_{\text{H}}$  from 0.64 to 0.82 ML with scan rate is evident however the increase also correlates with the shift to more negative vertex potentials where an increase in  $\text{H}_{\text{ads}}$

coverage is predicted by theory.<sup>33</sup> More negative vertex potentials were used to ensure that the transition between hydride formation and bulk HER was reached when using faster scan rates.

The impact of extended polarization at negative potentials where the hydride is formed was examined by voltammetry where the initial potential was held at  $-0.325$  and  $-0.35$  V for 30 s, respectively. As shown in Figure 3 the voltammetric kinetics of hydride decomposition following extended polarization at negative potentials are substantially faster than seen for voltammetry initiated at positive potentials on a hydride-free surface, i.e., Figures 1 and 2. Following pretreatment at  $-0.325$  V, Figure S8, the peak potentials for the first oxidative wave and EC-MS hydride decomposition are downshifted to  $0.126$  V ( $\approx 34 \mu\text{C cm}^{-2}$  or  $\approx 0.35 \text{ nmol cm}^{-2}$ ) and  $\approx 0.135$  V ( $1.59 \text{ nmol cm}^{-2}$ ), respectively. For pretreatment at a slightly more negative potential of  $-0.35$  V, the respective peaks in Figure 3 are downshifted further to  $0.107$  V ( $\approx 28 \mu\text{C cm}^{-2}$  or  $\approx 0.29 \text{ nmol cm}^{-2}$ ) and  $\approx 0.118$  V ( $1.29 \text{ nmol cm}^{-2}$ ), respectively. For both sets of experiments, the subsequent voltammograms with continuous scanning yield the same positive shift in peak positions to  $\approx 0.165$  and  $\approx 0.175$  V, respectively. If the oxidative charge is ascribed solely to  $\text{H}_{\text{ads}}$  oxidation to hydronium while the  $\text{H}_2$  flux is assigned to  $\text{H}_{\text{ads}}$  desorption by recombination the summation gives a fractional  $\text{H}_{\text{ads}}$  coverage of  $0.66$  ML at  $-0.325$  V and  $0.75$  ML at  $-0.350$  V, subject to the scan rate used. These values are well aligned with the predicted potential-dependent coverage from theoretical calculations detailed earlier.<sup>33</sup> Accordingly, excursions to more negative values lead to higher  $\text{H}_{\text{ads}}$  coverages and H-induced reconstruction of the Cu(111) that collectively impact the onset and acceleration of the HER. For subsequent cycles, the maximum  $\text{H}_{\text{ads}}$  coverage evaluated from the voltammograms decreased to  $(0.6 \pm 0.01)$  ML, Figure 3, and  $(0.54 \pm 0.015)$  ML, Figure S8, respectively, which reflect kinetic hindrance in hydride formation during voltammetric cycling. At more negative potentials where the coverage exceeds  $0.75$  ML, theory predicts a reconstruction of the existing  $(4 \times 4)$  structure with the formation of adatoms, dimers, and related vacancy structures that maintain the  $(4 \times 4)$  periodicity.<sup>33</sup> The adatoms and vacancies facilitate both higher  $\text{H}_{\text{ads}}$  coverage and enhanced reaction kinetics. Recent computational work indicates that adsorbed H is required and works synergistically with CO to create sites of CO-bound Cu atoms that sit  $0.1$  nm above the top surface accounting for surface reconstruction that accompanies  $\text{CO}_2\text{RR}$ .<sup>39</sup> The increased  $\text{H}_{\text{ads}}$  coverage and enhanced hydride decomposition and oxidation characteristics following aging, Figures 3 and S8, and/or during excursions to more negative potentials,  $< -0.325$  V, Figure 2, are consistent with this picture.

**Chronoamperometric EC-MS Measurements in  $0.1 \text{ mol L}^{-1} \text{HClO}_4$ .** Potential pulse EC-MS measurements were used for a more complete quantitative analysis of the transient and steady-state behavior associated with surface hydride formation and decomposition.<sup>36</sup> The experiment involved stepping the potential from an initial rest state,  $E_{\text{Rest}} = 0.175$  V to a more negative potential,  $E_{\text{Pulse}}$  for 2 min and then stepping back to  $E_{\text{Rest}}$  for 2 min. The  $E_{\text{Pulse}}$  value was then progressively advanced in  $-25$  mV increments (Figures 4 and S1). The chronoamperometric experiment mitigates convolution of the  $\text{H}_2$  diffusional lag from the dynamic potential scan used in voltammetry. Sequential chronoamperometric transients for each pulse cycle between  $E_{\text{Pulse}}$  and  $E_{\text{Rest}}$  in He-saturated  $0.1 \text{ mol L}^{-1} \text{HClO}_4$  electrolyte are superimposed in Figure 4a. Starting

from  $E_{\text{Pulse}}$  of  $-0.05$  V, the steady-state current densities at  $E_{\text{Pulse}}$  and  $E_{\text{Rest}}$  remain roughly  $< -5 \mu\text{A cm}^{-2}$  and  $\approx -2 \mu\text{A cm}^{-2}$ , respectively. These negative currents arise from the oxygen reduction reaction (ORR) due to trace (on the order of  $\text{pmol L}^{-1} \text{s}^{-1}$ )  $\text{O}_2$  flux, possibly from leakage through various joints and connections of the EC-MS cell, as no change in  $\text{H}_2$  flux was detected via the mass spectrometer (Figure 4b).<sup>36</sup> The current density when  $E_{\text{Pulse}} = -0.1$  V increases to  $\approx -5.5 \mu\text{A cm}^{-2}$ , consistent with an increase in the steady-state HER rate (Figure S9). Stepping to  $-0.150$  V increases the steady-state HER rate modestly, although a notable change in the first  $\approx 25$  s of the current transient is observed (Figures 4b and S9). Compared to  $-0.150$  V, the time to reach a steady-state current increases at  $-0.175$  and  $-0.200$  V before decreasing for  $E_{\text{Pulse}} \geq -0.225$  V. The slower time constant for the  $-0.150$  and  $-0.225$  V transients is associated with the nucleation and growth of the surface hydride phase superimposed on proton reduction to  $\text{H}_2$  and double-layer charging. An additional contribution from anion desorption is possible although this is believed to be unlikely for perchlorate electrolytes in contrast to the measurable influence of sulfate, phosphate, or chloride ions.<sup>36</sup> Pulses in the  $100 \mu\text{mol L}^{-1} \text{HCl} + 0.1 \text{ mol L}^{-1} \text{HClO}_4$  electrolytes show similar behavior albeit shifted negatively  $\approx -75$  mV due to inhibition of hydride formation by the adsorbed chloride (Figure S10). This results in a more convoluted current transient (left inset of Figure S10a) that involves the dynamics and additional charge necessarily associated with the sequence of  $\text{Cl}^-$  desorption and the formation of hydride. Comparing the transient charge at a pulse potential of  $-0.3$  V ( $-288$  vs  $-253 \mu\text{C cm}^{-2}$  for  $\text{Cl}^-$  vs  $\text{HClO}_4$ , vide infra) reveals  $-35 \mu\text{C cm}^{-2}$  of additional charge due to  $\text{Cl}^-$  desorption. Likewise, hydride formation in  $0.1 \text{ mol L}^{-1} \text{H}_2\text{SO}_4$  involved a transient charge of  $-275 \mu\text{C cm}^{-2}$  where the excess charge relative to  $0.1 \text{ mol L}^{-1} \text{HClO}_4$  is attributed to sulfate desorption (Figure 5a in ref 36).

Upon returning to  $E_{\text{Rest}}$  an oxidative transient current is observed (Figure 4a right inset), with the duration and charge increasing as the potential is stepped from more negative  $E_{\text{Pulse}}$  values between  $-0.05$  to  $-0.225$  V. The oxidative charge reflects a combination of double-layer charging, anion adsorption, and/or hydride decomposition by oxidation to hydronium. As noted above, although anion adsorption on Cu surfaces is well established for sulfate or halide electrolytes, evidence for specific perchlorate anion adsorption is at best ambiguous. Significantly, a recent STM study of a water-dosed Cu(111) surface in cryogenic vacuum environment revealed ordered adlayers that were ascribed to water and hydronium structures, a subset of which were similar to those observed in ECSTM studies.<sup>40,46–48</sup> Inspection of the oxidative current transients at  $E_{\text{Rest}}$  reveals that the time to reach the steady-state background current increases from 5 to 20 s as  $E_{\text{Pulse}}$  is made more negative. However, when  $E_{\text{Pulse}} < -0.225$  V an inversion and decrease in the time constant is evident with the transient lifetime dropping to 15 s following polarization at  $E_{\text{Pulse}}$  of  $-0.3$  V. The acceleration of the oxidative process (in  $0.1 \text{ mol L}^{-1} \text{HClO}_4$ ) following more negative pulse potentials is consistent with that seen in the related voltammetric experiments, Figures 3 and S8. One possible explanation is that Cu adatom formation driven by higher hydride coverages formed at more negative potentials leads to accelerated hydride decomposition with the step back to the rest potential.

Interestingly, the accelerated hydride decomposition seen in  $0.1 \text{ mol L}^{-1} \text{HClO}_4$  is not evident following titration with  $100 \mu\text{mol L}^{-1} \text{Cl}^-$ , nor is it evident in prior sulfuric acid experiments.

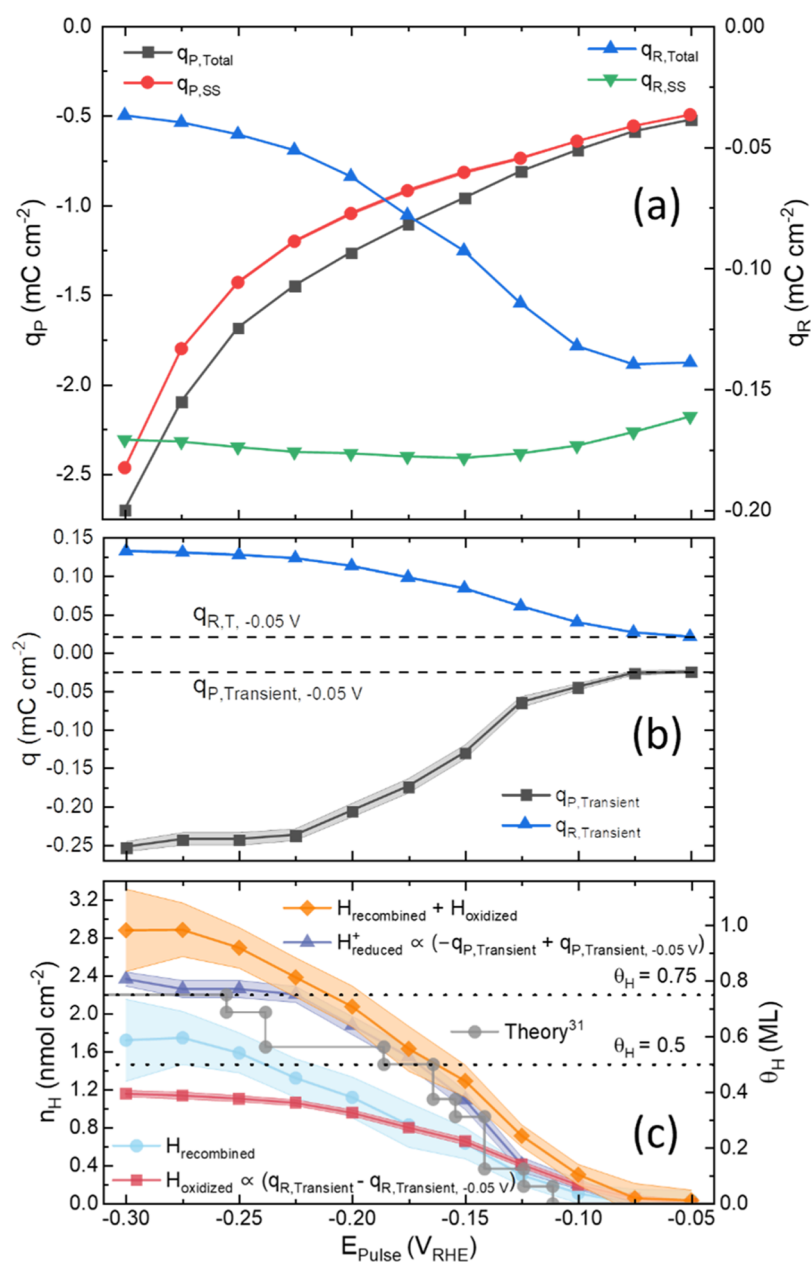


**Figure 5.** (a) Total ( $q_{P,\text{Total}}$  and  $q_{R,\text{Total}}$ ) and steady-state ( $q_{P,\text{SS}}$  and  $q_{R,\text{SS}}$ ) chronoamperometric charge and (b) their difference, the transient charge ( $q_{P,\text{Transient}}$  and  $q_{R,\text{Transient}}$ ), for  $E_{\text{Pulse}}$  and  $E_{\text{Rest}}$  during negative step potential pulse measurements in 0.1 mol L<sup>-1</sup> HClO<sub>4</sub> (Figure 4). (c) Total H coverage determined from either the background corrected hydronium reduction wave,  $H_{\text{reduced}}^+$ , or the sum of hydride recombination,  $H_{\text{recombined}}$ , and  $H_{\text{ads}}$  oxidation to hydronium,  $H_{\text{oxidized}}$ . The transparent background for each curve represents the standard deviation. Also plotted is the coverage (denoted as “theory” in the legend) predicted by computational simulations from Cheng et al. for pH 1 electrolyte.<sup>33</sup>

In the presence of Cl<sup>-</sup> the oxidative current transient increases abruptly when  $E_{\text{pulse}}$  is -0.2 V and effectively saturates for  $E_{\text{pulse}} < -0.225$  V consistent with completion of the hydride phase over a small potential window (Figure S10a and right inset). Also of interest, the oxidative current transients in the presence of Cl<sup>-</sup> (Figure S10b) do not accelerate when stepping from more negative potentials, e.g., -0.3 V, in contrast to that observed in pure 0.1 mol L<sup>-1</sup> HClO<sub>4</sub>. This might be attributed to anion-facilitated quenching of the elevated adatom population associated with the hydride phase formed at more negative potentials.

Following 120 s of polarization at  $E_{\text{pulse}}$  the potential is stepped back to  $E_{\text{Rest}}$  and the increase in H<sub>2</sub> flux provides an unambiguous signature of hydride formation by virtue of its

decomposition via H recombination to H<sub>2</sub> at  $E_{\text{Rest}}$  (Figure 4b and right inset). Notably, this occurs well positive of 0.0 V. The hydride decomposition peak at  $E_{\text{Rest}}$  continues to grow as  $E_{\text{pulse}}$  is stepped more negative with the integrated H<sub>2</sub> flux as a function of  $E_{\text{pulse}}$  shown in Figure S11. An inflection, evident near -0.225 V, is suggestive of a plateau or phase boundary in the  $H_{\text{ads}}$  coverage. Hydride formation at  $E_{\text{pulse}}$  overlaps the onset and development of HER with the latter reaching a steady-state rate within the first 30 s of the 120 s dwell period. This decay rate is accelerated substantially in the presence of Cl<sup>-</sup> with its strong absorption stimulating  $H_{\text{ads}}$  recombination to occur in nearly half of the time (10 s) for all pulse potentials (Figure S10b). This observation also supports the attribution of the sluggish decay curve, in the absence of halide, to the slow decomposition

kinetics of hydride rather than  $H_2$  diffusion across the thin layer of the electrolyte. In pure  $0.1 \text{ mol L}^{-1} \text{ HClO}_4$  and  $E_{\text{pulse}} < -0.2 \text{ V}$ , the additional increase in peak height upon stepping to  $E_{\text{rest}}$  partly reflects an increase in  $H_{\text{ads}}$  coverage but is convolved with residual  $H_2$  diffusing across the electrolyte following steady-state HER at  $E_{\text{pulse}}$  (Figure S11). The decay associated with this residual  $H_2$  significantly affects the shape of the hydride envelope. Quantitative analysis is further complicated by the competitive, first-order oxidation of  $H_{\text{ads}}$  to  $H_3O^+$ . Nonetheless, the more rapid decay in  $H_2$  flux following polarization at  $E_{\text{pulse}}$  values  $< -0.275 \text{ V}$  speaks to an increase in the kinetics for  $H_{\text{ads}}$  recombination and/or the  $H_{\text{ads}}$  oxidation reaction. The acceleration is most likely related to H-induced reconstruction of the surface that results in more reactive low-coordinate Cu adatoms at higher  $H_{\text{ads}}$  coverages.<sup>33</sup>

**Quantitative Analysis of Hydride Coverage.** The hydride coverage can be quantified using the steady-state approximation for the HER, as done previously in similar experiments with sulfuric acid electrolyte.<sup>36</sup> In contrast to experiments in sulfate- or chloride-containing media, chemisorption of perchlorate is negligible with no order anion layers reported in the plurality of ECSTM studies therefore, no charge will be assigned to anion adsorption.<sup>40,47</sup> For chronoamperometry, separating the steady-state charge ( $q_{\text{P,SS}}, q_{\text{R,SS}}$ ) from the total measured charge ( $q_{\text{P,Total}}, q_{\text{R,Total}}$ ) for both  $E_{\text{pulse}}$  and  $E_{\text{rest}}$  (Figure 4a,b), isolates the transient charges ( $q_{\text{P,Transient}}, q_{\text{R,Transient}}$ ) associated with reductive hydride formation at  $E_{\text{pulse}}$  and its subsequent oxidation at  $E_{\text{rest}}$ , respectively. The steady-state HER approximation is evaluated by averaging the current over the final 60 s of  $E_{\text{pulse}}$  or  $E_{\text{rest}}$  and multiplying by the total pulse or rest time (120 s each) to obtain the charge ( $q_{\text{P,SS}}, q_{\text{R,SS}}$ ). As shown in Figure 5, the approximated steady-state charge during  $E_{\text{pulse}}$  or  $E_{\text{rest}}$  is subtracted from the total measured charge to yield the transient charge,  $q_{\text{P, Transient}}$  or  $q_{\text{R, Transient}}$ , respectively. Initially, for  $E_{\text{pulse}} \geq -0.175 \text{ V}$ , the transient charges for  $E_{\text{pulse}}$  and  $E_{\text{rest}}$  are approximately equal to opposite polarity, congruent with reversible capacitive charging of the interface. The onset of hydride formation introduces asymmetry in the net transient charge, as captured in Figure 5b. Specifically,  $|q_{\text{P, Transient}}/q_{\text{R, Transient}}|$  increases from around 1 at  $E_{\text{pulse}} = -0.05 \text{ V}$  (prehydride formation) to a plateau of  $\approx 2$  at  $-0.225 \text{ V}$ , due to surface hydride formation. This charge analysis ignores the contribution of double-layer capacitance associated with stepping between  $E_{\text{pulse}}$  to  $E_{\text{rest}}$ . However, negligible hydride formation occurs prior to  $-0.05 \text{ V}$  and thus an upper bound for the corresponding net change associated with hydride formation is evaluated based on the difference between the transient charge at  $-0.05 \text{ V}$  (hydride-free) and  $-0.225 \text{ V}$  (hydride-covered), giving  $(-218 \pm 8) \mu\text{C cm}^{-2}$  of charge to reduce  $H^+$  to surface hydride (Figure 5c). Normalizing this charge to  $\theta_{\text{H}}$  on Cu(111) yields a saturated coverage of  $(0.77 \pm 0.03) \text{ ML}$ . Assuming that the decomposition of surface hydride is a competitive process between oxidation and recombination reactions, the contribution of oxidation can be determined by measuring the background corrected oxidation charge when stepping from  $E_{\text{pulse}}$  to  $E_{\text{rest}}$ . At its maximum, this yields  $\Delta q_{\text{R, Transient}}$  ( $103 \pm 2$ )  $\mu\text{C cm}^{-2}$  (Figure 5b) that corresponds to a loss of  $(0.36 \pm 0.01) \text{ ML}$  of H (Figure 5c). The contribution from the H recombination process is evaluated directly from the 2 amu EC-MS measurement.

Analysis of the  $H_2$  flux also involves partitioning the measured  $H_2$  ( $H_{2,\text{Total}}$ ) into contributions from the HER ( $H_{2,\text{HER}}$ ) and hydride decomposition by H recombination ( $H_{2,\text{Hydride}}$ ) (Figure

S12). Previous work utilized the total collection capacity of the EC-MS platform<sup>41</sup> to deconvolve these terms. It was assumed that steady-state HER at  $E_{\text{pulse}}$  is rapidly (instantly) attained, with the EC-MS detection delayed due to  $H_2$  diffusion across the thin electrolyte layer.<sup>36</sup> The EC-MS measurement is particularly effective in revealing the onset of hydride formation as the HER at  $E_{\text{rest}}$  drops rapidly to zero while the  $H_{\text{ads}}$  recombination to yield  $H_2$  takes several seconds, Figures 4b, S9, and S11. The integrated result of the small  $H_2$  quantity detected, following polarization at  $-75 \text{ mV}$ , is consistent with assigning the transient charge at  $-0.05 \text{ V}$  to the capacitance, Figure 5b. Integration of the decomposition peak upon stepping to  $E_{\text{rest}}$  shows a monotonic relationship between hydride coverage and  $E_{\text{pulse}}$  between  $-0.10$  to  $-0.25 \text{ V}$ , Figure 5c. A plateau is evident between  $-0.25$  and  $-0.3 \text{ V}$ , corresponding to a hydride coverage of  $(0.54 \pm 0.05) \text{ ML}$ . This is lower than the  $0.67 \text{ ML}$  observed in  $0.1 \text{ mol L}^{-1} \text{ H}_2\text{SO}_4$  using the same procedures which reflects the role of sulfate adsorption in spurring the recombination reaction.<sup>36</sup>

Deconvolving the charge contributions during negative potential pulses in  $100 \mu\text{mol L}^{-1} \text{ HCl} + 0.1 \text{ mol L}^{-1} \text{ HClO}_4$  (Figure S13) requires consideration of  $\text{Cl}^-$  desorption during hydride formation and  $\text{Cl}^-$  adsorption during hydride decomposition. As noted earlier, the charge associated with hydride formation in the presence of  $\text{Cl}^-$  exceeds that for neat perchloric acid by  $\approx 35 \mu\text{C cm}^{-2}$ . Studies of  $\text{Cl}^-$  adsorption on Ag(111) indicate an electrosorption valency of 0.44 and based on the similarity between the  $pzc$  of Cu and Ag this value is adopted.<sup>49</sup> Accordingly, the excess charge of  $\approx 35 \mu\text{C cm}^{-2}$  corresponds to a fractional  $\text{Cl}^-$  coverage  $\theta_{\text{Cl}}$  of 0.28 ML compared to 0.33 ML expected for a  $(\sqrt{3} \times \sqrt{3})R30^\circ$  overlayer structure that can be taken as a first-order estimate based on reported adlayer surface structures.<sup>44,50</sup> Alternatively, an inverse analysis using the electrosorption normalized charge for the  $(\sqrt{3} \times \sqrt{3})R30^\circ$  adlayer of  $\approx 41 \mu\text{C cm}^{-2}$  can be used to provide a charge-based estimate of the hydride coverage at  $-0.35 \text{ V}$ ,  $\theta_{\text{H}}$  of 0.89, not surprising since double-layer charge was not considered. It should also be noted that the coexistence of H and Cl adlayer structures proposed in recent theory might lead to variation in the electrosorption valency that will need to be considered.<sup>51</sup> Meanwhile the  $\theta_{\text{H}}$  determined by integration of  $H_2$  flux during desorption in the presence of  $\text{Cl}^-$  appears to converge to 0.75 ML (Figure S13c), while that for perchloric acid does not exceed 0.6 ML, supporting the idea that Cl adsorption favors H recombination over oxidation.

In the absence of anion adsorption, the sum of the oxidative and recombination components associated with hydride decomposition measured at  $E_{\text{rest}}$  can be compared with the proton reduction charge used to form the hydride (Figure 5c). Good agreement between the metrics is achieved for  $\geq -0.225 \text{ V}$  where  $\approx 0.75 \text{ ML}$  of  $H_{\text{ads}}$  is expected. This is further corroborated by the 0.75 ML of H measured through recombination when  $100 \mu\text{mol L}^{-1} \text{ HCl}$  is present in  $0.1 \text{ mol L}^{-1} \text{ HClO}_4$ . At more negative potentials, the transient charge at  $E_{\text{pulse}}$  plateaus, whereas the sum of oxidation and recombination increases slightly to  $\approx 1 \text{ ML}$  by  $-0.3 \text{ V}$ . However, this is accompanied by an increase in standard deviation that weakens the significance of the increase. Recent computational studies of H adsorption on Cu(111) indicate two domains of hydride stability with a coverage of 0.56 and 0.75 ML that correspond to slightly different  $(4 \times 4)$  periodic structures similar to that observed by ECSTM.<sup>33</sup> The predicted coverage (Figure 5c, "Theory") overlaps the present and previous EC-MS studies in

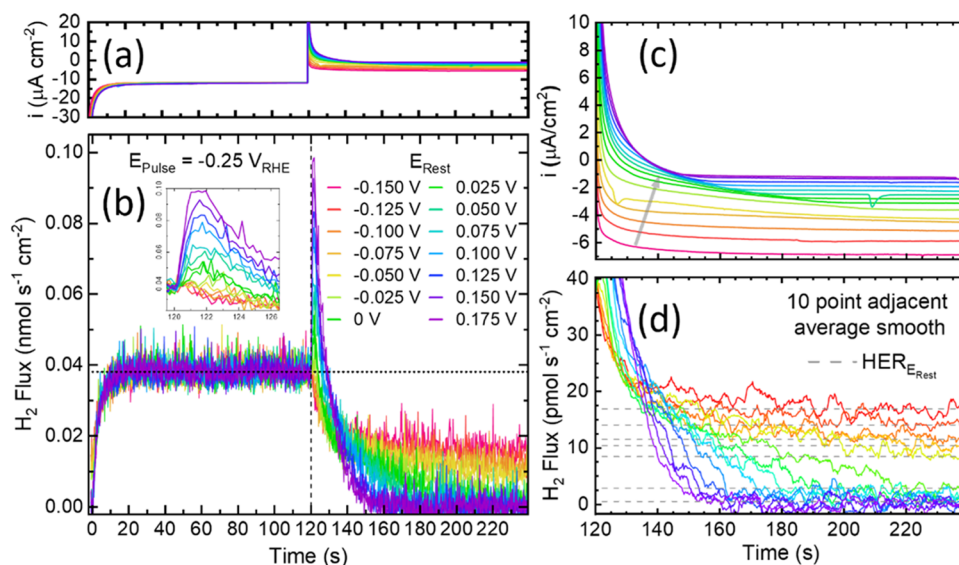


**Figure 6.** (a, c) Chronoamperometry and (b, d)  $\text{H}_2$  flux during variable  $E_{\text{Rest}}$  measurements on Cu(111) in  $0.1 \text{ mol L}^{-1} \text{ HClO}_4$ . The inset in (b) magnifies the 2 amu hydride decomposition peak, while the magnified current and  $\text{H}_2$  flux profile for the entire  $E_{\text{Rest}}$  cycle are presented in (c) and (d), respectively. The horizontal dashed line in (b) represents the average steady-state  $\text{H}_2$  flux during the  $E_{\text{Pulse}}$ . The gray dashed lines in (d) reflect the steady-state HER rate at  $E_{\text{Rest}}$  found by averaging the last 5 s of the  $\text{H}_2$  flux for each  $E_{\text{Rest}}$ .

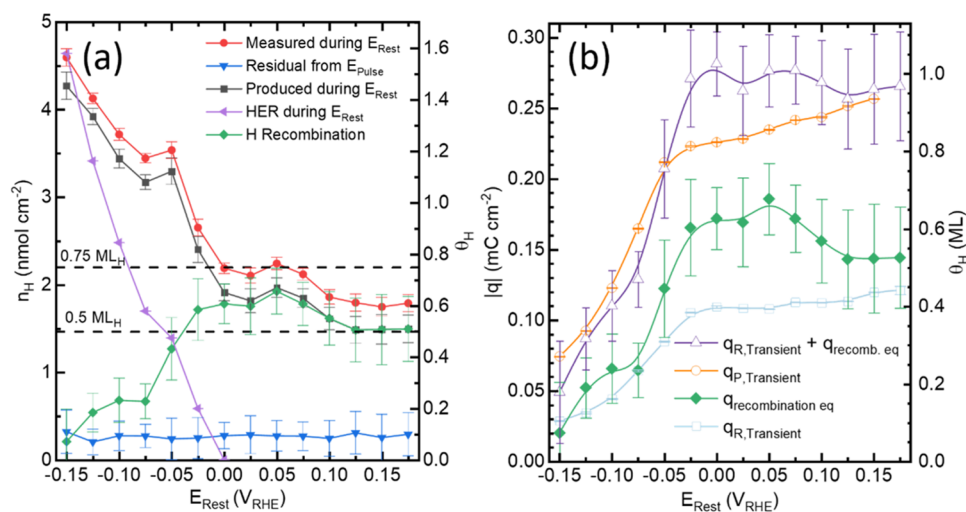


**Figure 7.** (a) Total and partitioned quantities of  $n_{\text{H}}$  determined via the EC-MS and (b) charge analysis from (Figure 6a) as a function of  $E_{\text{Rest}}$ . The  $q_{\text{recombination eq}}$  (green diamonds) in (b) is the hydride charge equivalent that is not realized due to the loss of  $\text{H}_2$  by recombination, as measured by EC-MS (a). The error bars represent the standard deviation of the measurement.

perchloric and sulfuric acid. The chief distinction between sulfuric acid, hydrochloric acid, and perchloric acid is the strength of anion adsorption; specifically, sulfate and/or chloride adsorption favors hydride decomposition by recombination, whereas the absence of perchlorate adsorption results in a measurable increase in the amount of  $\text{H}_{\text{ads}}$  removed by oxidation.

**Impact of  $E_{\text{Rest}}$  on Hydride Decomposition**  $0.1 \text{ mol L}^{-1} \text{ HClO}_4$ . To further explore hydride decomposition and its partitioning between  $\text{H}_{\text{ads}}$  recombination to  $\text{H}_2$  versus oxidation to hydronium, a similar set of pulse experiments were performed where  $E_{\text{rest}}$  was changed as  $E_{\text{Pulse}}$  was held constant (Figure 6). For this experiment,  $E_{\text{Pulse}}$  was chosen to be  $-0.25 \text{ V}$ , which corresponds to the well-defined plateau in hydride coverage established in the previous experiment. The detailed potential program is shown in Figure S2 with the substrate initially poised at  $0.175 \text{ V}$ , where the surface is known to be hydride-free. The

chronoamperometric, Figure 6a, and  $\text{H}_2$  flux, Figure 6b, measurements during repetitive stepping to  $E_{\text{Pulse}}$  of  $-0.25 \text{ V}$  demonstrate good reproducibility while the choice of  $E_{\text{Rest}}$  significantly impacts the rate and nature of hydride decomposition. For the first  $E_{\text{Rest}}$  value of  $-0.15 \text{ V}$  both current and  $\text{H}_2$  flux decay to a new steady-state HER value (Figure 7a “HER During  $E_{\text{Rest}}$ ”). As  $E_{\text{Rest}}$  is sequentially increased in  $+25 \text{ mV}$  increments, up to  $-0.025 \text{ V}$  the current and  $\text{H}_2$  flux transients become more sluggish. Once  $E_{\text{Rest}} > -0.025 \text{ V}$  a clear uptick in  $\text{H}_2$  flux (inset shown in Figure 6b) from hydride decomposition by recombination accompanies the step from  $E_{\text{Pulse}}$  to  $E_{\text{Rest}}$ . At the same time a slow transient oxidative process is observed in Figure 6c that reflects the tail of double-layer charging and  $\text{H}_{\text{ads}}$  oxidation to hydronium relaxes, decaying over  $\approx 80 \text{ s}$  at  $-0.025 \text{ V}$  (compared to  $\approx 30 \text{ s}$  at  $0.175 \text{ V}$ ), to a steady-state reduction current associated with residual oxygen.

Advancing  $E_{\text{Rest}}$  further leads to acceleration of hydride decomposition with the  $\text{H}_2$  flux reaching the  $0 \text{ nmol s}^{-1} \text{ cm}^{-2}$  baseline well within the 120 s duration for all  $E_{\text{Rest}} > -0.025 \text{ V}$ . The  $0 \text{ nmol s}^{-1} \text{ cm}^{-2}$  baseline is helpful in quantifying the HER kinetics that are otherwise obscured by the residual oxygen reduction reaction. Indeed, the  $\text{H}_2$  flux approaches zero at  $0.0 \text{ V}$ , consistent with this idea. Direct comparison between the current density and  $\text{H}_2$  flux at the end of  $E_{\text{Rest}}$  is shown in Figure S14 consistent with a residual oxygen reduction reaction current that increases from  $1.5 \mu\text{A/cm}^2$  at  $0.175 \text{ V}$  to reach a transport-limited value of  $\approx 3.0 \mu\text{A/cm}^2$  near  $0.0 \text{ V}$ . Integration of the  $E_{\text{Pulse}}$  current transient at  $-0.250 \text{ V}$  following the initial step from an  $E_{\text{Rest}}$  of  $0.175 \text{ V}$  and applying the steady-state HER approximation yields  $0.246 \text{ mC cm}^{-2}$  of transient charge, in good agreement with the early negative step potential pulse measurements (Figure 5b). This charge equates to a  $\text{H}_{\text{ads}}$  coverage of  $0.78 \text{ ML}$  based on the strategy used to determine  $\text{H}_{\text{reduced}}^+$  in Figure 5c.

As in earlier EC-MS analyses, the steady-state and total collection approximation is used to account for the different sources of  $\text{H}_2$  measured during  $E_{\text{Rest}}$ . This includes not only  $\text{H}_{\text{ads}}$  desorption via recombination but also ongoing HER at  $E_{\text{Rest}}$  along with the collection of  $\text{H}_2$  produced during  $E_{\text{Pulse}}$  but measured during  $E_{\text{Rest}}$  due to diffusional lag. The integrated  $\text{H}_2$  flux over the duration of  $E_{\text{Rest}}$  is given as “Measured during  $E_{\text{Rest}}$ ” in Figure 7a. The contribution of  $\text{H}_2$ , due to diffusional lag from the HER at  $E_{\text{Pulse}}$ , “Residual from  $E_{\text{Pulse}}$ ” is estimated by subtracting the total  $\text{H}_2$  measured during  $E_{\text{Pulse}}$  from the product of the steady-state  $\text{H}_2$  flux and pulse time at  $E_{\text{Pulse}}$  (Figure S15). This “Residual from  $E_{\text{Pulse}}$ ” is then subtracted from the “Measured during  $E_{\text{Rest}}$ ” to leave the contribution “Produced during  $E_{\text{Rest}}$ ” attributed to H recombination and HER as summarized in Figure 7a. Separation of  $\text{H}_2$  generated from  $\text{H}_{\text{ads}}$  recombination versus HER at  $E_{\text{Rest}}$  can be approximated by assuming that the last 5 s of the EC-MS transient is representative of a steady-state HER flux (Figures 6d and S14) that multiplied by  $t_{\text{Rest}}$  gives the contribution “HER during  $E_{\text{Rest}}$ ” shown in Figure 7a. The approach works well, although close inspection of the  $E_{\text{Rest}}$  transients between  $-0.1$  and  $-0.025 \text{ V}$  indicates the slow rate of H recombination may overlap with the 5 s averaging evaluation of the HER contribution (Figure 6d). With that qualification, subtraction of “HER during  $E_{\text{Rest}}$ ” from “Produced during  $E_{\text{Rest}}$ ” yields the amount of  $\text{H}_2$  generated by hydride decomposition via the recombination pathway as indicated by “H Recombination” in Figure 7a.

The analysis indicates a near monotonic dependence of  $\text{H}_{\text{ads}}$  desorption by recombination as  $E_{\text{Rest}}$  is increased from  $-0.15$  to  $-0.025 \text{ V}$ . As  $E_{\text{Rest}}$  is increased further from  $-0.025$  and  $0.075 \text{ V}$ , the amount of  $\text{H}_{\text{ads}}$  desorbed by recombination rises to reach a maximum near  $0.6 \text{ ML}$  before settling to a value near  $0.5 \text{ ML}$  for  $E_{\text{Rest}} > 0.125$ . As the total amount of hydride to be decomposed is fixed, the transition or decrease in the amount desorbed by recombination is attributed to the onset of the oxidative removal of  $\text{H}_{\text{ads}}$  as hydronium. This is consistent with  $E_{\text{Rest}}$  becoming greater than  $0 \text{ V}$ . Interestingly the transition also overlaps with the potential range where two minor peaks develop during cyclic voltammetric experiments as shown in Figure 1. The kinetic limitations on hydride decomposition are such that in voltammetric experiments the peak reaction is observed at much more positive potentials. For chronoamperometry, the potential and the time dependence are well captured by the  $\text{H}_2$  signal (Figure 6d) where hydride decomposition takes  $\approx 100 \text{ s}$  at  $-0.05 \text{ V}$  but only requires  $40 \text{ s}$  at  $0.075 \text{ V}$ . The trend continues at

higher  $E_{\text{Rest}}$  with the transition taking only  $\approx 20 \text{ s}$  at  $0.175 \text{ V}$  which is convolved with the time required for  $\text{H}_2$  to diffuse across the electrolyte to the MS entry port.

The charge transients ( $q_{\text{P,Transient}}$  and  $q_{\text{R,Transient}}$ ) for the positive step potential pulse measurements (Figure 7b) were determined by following the same strategy used for the negative step potential pulse measurements, where the steady-state charge was subtracted from the total charge (Figure S16) for both  $E_{\text{Pulse}}$  and  $E_{\text{Rest}}$ . The steady-state currents were determined by averaging the current for the final 3 s of  $E_{\text{Pulse}}$  and  $E_{\text{Rest}}$  respectively, and the charge was found by multiplying by the time of the pulse or rest (120 s each). As with the EC-MS analysis this assumes the steady-state processes are not influenced by transient events at the electrode surface. This may be a less accurate procedure for assessing the current compared to  $\text{H}_2$  flux, given that other phenomena may contribute such as parasitic ORR, double-layer, and/or adsorption-related pseudocapacitance. The experiment begins by first forming a hydride at  $-0.250 \text{ V}$  that yields a  $q_{\text{P,Transient}}$  of  $-0.246 \mu\text{C/cm}^2$  (not indicated in Figure 7b). For the first positive  $E_{\text{Rest}}$  step to  $-0.15 \text{ V}$  the  $q_{\text{R,Transient}}$  is only  $30 \mu\text{C cm}^{-2}$ . This increases to nearly  $110 \mu\text{C cm}^{-2}$  for an  $E_{\text{Rest}}$  of  $-0.025 \text{ V}$  with only modest increases thereafter. The  $q_{\text{P,Transient}}$  associated with the next  $E_{\text{Pulse}}$  corresponds to reforming the increment of hydride decomposed on the previous  $E_{\text{Rest}}$  step. Assuming the reformed hydride phase after each  $E_{\text{Pulse}}$  is the same, the difference between  $q_{\text{P,Transient}}$  (e.g., the charge for hydride formation) and its subsequent oxidative decomposition must equal the amount of hydride decomposed through the recombination to  $\text{H}_2$ . The materials balance is examined by converting  $n_{\text{H}}$  from recombination (“H Recombination” Figure 7a) to its charge equivalent,  $q_{\text{recombined equivalent}}$ . Combining this with  $q_{\text{R,Transient}}$  for hydride decomposition by oxidation to hydronium enables a comparison to the hydride formation charge,  $q_{\text{P,Transient}}$ . Assuming the hydride structure is conserved over multiple formation-decomposition cycles the sum of the two decomposition pathways should equal the charge needed to reform the hydride. The combination shows that complete decomposition of the hydride phase occurs at potentials  $> -0.05 \text{ V}$ . Reasonable agreement between the charge and  $\text{H}_2$  flux measurements is encouraging especially considering the uncertainties in the charge analysis associated with residual oxygen reduction reaction, double-layer capacitance, and the assumption implicit in the steady-state analysis. Future exploration will focus on rectifying observed differences between chronoamperometry and EC-MS during potential pulse measurements. Of particular interest is the impact of anion adsorption on the partitioning of the decomposition reaction between oxidative desorption versus H recombination. Previous work with sulfuric acid indicated that strong anion chemisorption accelerates the rate of the recombination pathway, such that desorption is complete before the overpotential increases enough for the oxidative desorption channel to become significant. Conversely, the decrease in H recombination for  $E_{\text{Rest}} > 0.05 \text{ V}$  (Figure 7) points to a potential dependent increase in hydride oxidation.

Looking beyond hydride formation and decomposition to its effect on hydrogenation reactions, two distinctive regimes of behavior may emerge. In the first instance formation of the hydride overlaps the potential region where many hydrogenation reactions occur and the hydride phase itself may serve as the catalytic template but perhaps also as an active reaction.<sup>22,23</sup> A prime example for consideration is the reduction

of oxygen (ORR) where product selectivity between hydrogen peroxide versus water is known to be a sensitive function of anion adsorption and surface structure.<sup>52,53</sup> Indeed, the transitions in ORR product selectivity directly overlap the potential regime where hydride formation and decomposition occur motivating the need for further study.<sup>35,36,52,53</sup> A second regime of behavior to consider involves cross-coupling between potential-induced hydride formation and its desorption with the hydrogenation reaction of interest. An example of this is CO<sub>2</sub>/CO reduction on Cu surfaces using pulsed potential, or pulsed current, schemes where the perturbation repeatedly transits the hydride formation and decomposition window.<sup>17,54</sup> In this instance the binding energy of adsorbed hydrogen varies greatly during the process with hydride first being formed on the negative-going potential pulse while during the reverse step adsorbed hydrogen is available for further hydrogenation reactions but at a much lower energy cost.<sup>54</sup>

## CONCLUSIONS

Surface hydride formation on Cu(111) in perchloric acid is associated with two reductive waves. Chronoamperometry measurements support theoretical predictions of a domain of uniform hydride coverage near 0.75 ML exists between  $-0.225$  and  $-0.3$  V.<sup>33</sup> The inflection between the two voltammetric reduction waves is associated with reaching  $\approx 0.8$  ML of hydride followed by the onset of the HER. The latter is also congruent with computational predictions detailing the formation of low coordination sites that may be responsible for the increase in HER kinetics.<sup>33</sup> Variation of the scan rate in cyclic voltammetry reveals two additional minor peaks centered near  $-50$  mV likely associated with the destabilization/stabilization of the hydride phase. Above  $-0.050$  V the surface hydride undergoes decomposition either by H<sub>ads</sub> recombination to H<sub>2</sub> or by oxidation back to H<sub>3</sub>O<sup>+</sup>, the rate of the latter increasing with potential. Kinetic limitations of the oxidation reaction manifest in the displacement of the oxidation wave to higher potentials for higher voltammetric scan rates. This is also evident in chronoamperometry where compression of the q<sub>R</sub> time constants occurred as E<sub>Rest</sub> increased from  $-0.025$  to  $0.175$  V while the net oxidative charge was largely independent of the applied potential. Exposure to more negative potentials for longer times accelerates subsequent voltammetric hydride decomposition kinetics, presumably due to structural rearrangement and/or elevated H<sub>ads</sub> coverage. The overpotential required for hydride formation on Cu(111) may impact the onset of hydrogenation reactions. Likewise, the slow decomposition kinetics for hydride decomposition and the prospect of weakly bound H<sub>ads</sub> being available at more positive potentials have implications for the use of pulse potential activation of hydrogenation reactions.

## ASSOCIATED CONTENT

### Supporting Information

The Supporting Information is available free of charge at <https://pubs.acs.org/doi/10.1021/jacs.4c12782>.

The supporting information contains; continuous plots of the negative and positive potential pulse experiments, electrochemical impedance spectroscopy, cyclic voltammetry (CV) where scan rate was modulated without pausing, CVs with varying concentrations of HCl present in the electrolyte, versions of Figure 2 for additional scan rates, a table tabulating values from Figure 2 and Figure

S6, plots of maximum H coverage vs potential during CVs at different scan rates, CVs with negative potential holds prior to the first scan and corresponding H coverage, plots that zoom-in on current and H<sub>2</sub> flux during potential pulses, negative potential pulse experiments with HCl in the electrolyte, plots of integrated H<sub>2</sub> flux during E<sub>Rest</sub> of negative step potential pulse measurements, quantities of n<sub>H</sub> measured by the EC-MS during negative potential pulse measurements, charges from negative potential pulse measurements, steady-state current density from the last 5 s of E<sub>Rest</sub> during potential pulse measurements, total and steady-state H measured during E<sub>Pulse</sub> for positive step potential pulse measurements, and total or steady-state charges from E<sub>Pulse</sub> during positive step potential pulse measurements (PDF)

## AUTHOR INFORMATION

### Corresponding Authors

David Raciti – Materials Science and Engineering Division, National Institute of Standards and Technology, Gaithersburg, Maryland 20899, United States; [orcid.org/0000-0002-9580-4524](https://orcid.org/0000-0002-9580-4524); Email: [david.raciti@nist.gov](mailto:david.raciti@nist.gov)

Thomas P. Moffat – Materials Science and Engineering Division, National Institute of Standards and Technology, Gaithersburg, Maryland 20899, United States; [orcid.org/0000-0003-4377-1692](https://orcid.org/0000-0003-4377-1692); Email: [thomas.moffat@nist.gov](mailto:thomas.moffat@nist.gov)

Complete contact information is available at: <https://pubs.acs.org/10.1021/jacs.4c12782>

### Author Contributions

Official contribution of the National Institute of Standards and Technology; not subject to copyright in the United States.

### Notes

The authors declare no competing financial interest.

## ACKNOWLEDGMENTS

This work was performed with funding from the CHIPS Metrology Program, part of CHIPS for America, National Institute of Standards and Technology, U.S. Department of Commerce. We thank Sandra Young for help with metallographic preparation.

## ADDITIONAL NOTE

\*Certain commercial equipment, instruments, or materials are identified in this paper to specify the experimental procedure adequately. Such identification is not intended to imply recommendation or endorsement by the National Institute of Standards and Technology, nor is it intended to imply that the materials or equipment identified are necessarily the best available for the purpose.

## REFERENCES

- (1) Moffat, T. P.; Braun, T. M.; Raciti, D.; Josell, D. Superconformal Film Growth: From Smoothing Surfaces to Interconnect Technology. *Acc. Chem. Res.* **2023**, *56* (9), 1004–1017.
- (2) Chen, X.; Chen, J.; Alghoraibi, N. M.; Henckel, D. A.; Zhang, R.; Nwabara, U. O.; Madsen, K. E.; Kenis, P. J. A.; Zimmerman, S. C.; Gewirth, A. A. Electrochemical CO<sub>2</sub> -to-Ethylene Conversion on Polyamine-Incorporated Cu Electrodes. *Nat. Catal.* **2021**, *4* (1), 20–27.

- (3) Wang, H.; Huang, J.; Cai, J.; Wei, Y.; Cao, A.; Liu, B.; Lu, S. In Situ/Operando Methods for Understanding Electrocatalytic Nitrate Reduction Reaction. *Small Methods* **2023**, *7* (7), No. 23001169.
- (4) Butcher, D. P.; Gewirth, A. A. Nitrate Reduction Pathways on Cu Single Crystal Surfaces: Effect of Oxide and  $\text{Cl}^-$ . *Nano Energy* **2016**, *29*, 457–465.
- (5) Barrera, L.; Silcox, R.; Giammalvo, K.; Brower, E.; Isip, E.; Bala Chandran, R. Combined Effects of Concentration, pH, and Polycrystalline Copper Surfaces on Electrocatalytic Nitrate-to-Ammonia Activity and Selectivity. *ACS Catal.* **2023**, *13* (7), 4178–4192.
- (6) Fukumuro, N.; Adachi, T.; Yae, S.; Matsuda, H.; Fukai, Y. Influence of Hydrogen on Room Temperature Recrystallisation of Electrodeposited Cu Films: Thermal Desorption Spectroscopy. *Trans. IMF* **2011**, *89* (4), 198–201.
- (7) Amador, L. L.; Rolet, J.; Doche, M.-L.; Massuti-Ballester, P.; Gigandet, M.-P.; Moutarlier, V.; Taborelli, M.; Ferreira, L. M. A.; Chiggiato, P.; Hihn, J.-Y. The Effect of Pulsed Current and Organic Additives on Hydrogen Incorporation in Electroformed Copper Used in Ultrahigh Vacuum Applications. *J. Electrochem. Soc.* **2019**, *166* (10), No. D366.
- (8) Vaškėlis, A.; Juškė, R.; Jačiauskienė, J. Copper Hydride Formation in the Electroless Copper Plating Process: In Situ X-Ray Diffraction Evidence and Electrochemical Study. *Electrochim. Acta* **1998**, *43* (9), 1061–1066.
- (9) Lousada, C. M.; Fernandes, R. M. F.; Tarakina, N. V.; Soroka, I. L. Synthesis of Copper Hydride (CuH) from  $\text{CuCO}_3 \cdot \text{Cu}(\text{OH})_2$  – a Path to Electrically Conductive Thin Films of Cu. *Dalton Trans.* **2017**, *46* (20), 6533–6543.
- (10) Yin, D.; Murdoch, H. A.; Chad Hornbuckle, B.; Hernández-Rivera, E.; Dunstan, M. K. Investigation of Anomalous Copper Hydride Phase during Magnetic Field-Assisted Electrodeposition of Copper. *Electrochem. Commun.* **2019**, *98*, 96–100.
- (11) Fukumuro, N.; Tohda, K.; Yae, S. Existing States of Co-Deposited Hydrogen in Electrolessly Deposited Copper Films from EDTA Complex Bath. *J. Electrochem. Soc.* **2022**, *169* (12), No. 122505.
- (12) Dutta, A.; Rahaman, M.; Luedi, N. C.; Mohos, M.; Broekmann, P. Morphology Matters: Tuning the Product Distribution of  $\text{CO}_2$  Electroreduction on Oxide-Derived Cu Foam Catalysts. *ACS Catal.* **2016**, *6* (6), 3804–3814.
- (13) Otsuka, R.; Uda, M. Cathodic Corrosion of Cu in  $\text{H}_2\text{SO}_4$ . *Corros. Sci.* **1969**, *9* (9), 703–IN27.
- (14) Beamer, A. W.; Buss, J. A. Synthesis, Structural Characterization, and  $\text{CO}_2$  Reactivity of a Constitutionally Analogous Series of Tricopper Mono-, Di-, and Trihydrides. *J. Am. Chem. Soc.* **2023**, *145* (23), 12911–12919.
- (15) Deutsch, C.; Krause, N.; Lipshutz, B. H. CuH-Catalyzed Reactions. *Chem. Rev.* **2008**, *108* (8), 2916–2927.
- (16) Tang, Q.; Lee, Y.; Li, D.-Y.; Choi, W.; Liu, C. W.; Lee, D.; Jiang, D. Lattice-Hydride Mechanism in Electrocatalytic  $\text{CO}_2$  Reduction by Structurally Precise Copper-Hydride Nanoclusters. *J. Am. Chem. Soc.* **2017**, *139* (28), 9728–9736.
- (17) Timoshenko, J.; Bergmann, A.; Rettenmaier, C.; Herzog, A.; Arán-Ais, R. M.; Jeon, H. S.; Haase, F. T.; Hejral, U.; Grosse, P.; Kühl, S.; Davis, E. M.; Tian, J.; Magnussen, O.; Roldan Cuenya, B. Steering the Structure and Selectivity of  $\text{CO}_2$  Electroreduction Catalysts by Potential Pulses. *Nat. Catal.* **2022**, *5* (4), 259–267.
- (18) Amirbeigiarab, R.; Tian, J.; Herzog, A.; Qiu, C.; Bergmann, A.; Roldan Cuenya, B.; Magnussen, O. M. Atomic-Scale Surface Restructuring of Copper Electrodes under  $\text{CO}_2$  Electroreduction Conditions. *Nat. Catal.* **2023**, *6* (9), 837–846.
- (19) Cheng, D.; Nguyen, K.-L. C.; Sumaria, V.; Wei, Z.; Zhang, Z.; Gee, W.; Li, Y.; Morales-Guio, C. G.; Heyde, M.; Cuenya, B. R.; Alexandrova, A. N.; Sautet, P. Structure Sensitivity and Catalyst Restructuring for  $\text{CO}_2$  Electro-Reduction on Copper *ChemRxiv Catal.* **2024** DOI: 10.26434/chemrxiv-2024-z3dlp.
- (20) Wirtanen, T.; Prenzel, T.; Tessonnier, J.-P.; Waldvogel, S. R. Cathodic Corrosion of Metal Electrodes—How to Prevent It in Electroorganic Synthesis. *Chem. Rev.* **2021**, *121* (17), 10241–10270.
- (21) Bagger, A.; Ju, W.; Varela, A. S.; Strasser, P.; Rossmeisl, J. Electrochemical  $\text{CO}_2$  Reduction: A Classification Problem. *ChemPhysChem* **2017**, *18* (22), 3266–3273.
- (22) Ceyer, S. T. New Mechanisms for Chemistry at Surfaces. *Science* **1990**, *249* (4965), 133–139.
- (23) Ceyer, S. T. The Unique Chemistry of Hydrogen beneath the Surface: Catalytic Hydrogenation of Hydrocarbons. *Acc. Chem. Res.* **2001**, *34* (9), 737–744.
- (24) Abdellah, A. M.; Ismail, F.; Siig, O. W.; Yang, J.; Andrei, C. M.; DiCecco, L.-A.; Rakhsha, A.; Salem, K. E.; Grandfield, K.; Bassim, N.; Black, R.; Kastlunger, G.; Soleymani, L.; Higgins, D. Impact of Palladium/Palladium Hydride Conversion on Electrochemical  $\text{CO}_2$  Reduction via in-Situ Transmission Electron Microscopy and Diffraction. *Nat. Commun.* **2024**, *15* (1), No. 938.
- (25) Bennett, E.; Wilson, T.; Murphy, P. J.; Refson, K.; Hannon, A. C.; Imberti, S.; Callear, S. K.; Chass, G. A.; Parker, S. F. How the Surface Structure Determines the Properties of CuH. *Inorg. Chem.* **2015**, *54* (5), 2213–2220.
- (26) Mccash, E. M.; Parker, S. F.; Pritchard, J.; Chesters, M. A. The Adsorption of Atomic Hydrogen on Cu(111) Investigated by Reflection-Absorption Infrared Spectroscopy, Electron Energy Loss Spectroscopy and Low Energy Electron Diffraction. *Surf. Sci.* **1989**, *215* (3), 363–377.
- (27) Lamont, C. L. A.; Persson, B. N. J.; Williams, G. P. Dynamics of Atomic Adsorbates: Hydrogen on Cu(111). *Chem. Phys. Lett.* **1995**, *243* (5), 429–434.
- (28) Lee, G.; Plummer, E. W. High-Resolution Electron Energy Loss Spectroscopy Study on Chemisorption of Hydrogen on Cu(111). *Surf. Sci.* **2002**, *498* (3), 229–236.
- (29) Mudiyansele, K.; Yang, Y.; Hoffmann, F. M.; Furlong, O. J.; Hrbek, J.; White, M. G.; Liu, P.; Stacchiola, D. J. Adsorption of Hydrogen on the Surface and Sub-Surface of Cu(111). *J. Chem. Phys.* **2013**, *139* (4), No. 044712.
- (30) Korzhavyi, P. A.; Soroka, I. L.; Isaev, E. I.; Lilja, C.; Johansson, B. Exploring Monovalent Copper Compounds with Oxygen and Hydrogen. *Proc. Natl. Acad. Sci. U.S.A.* **2012**, *109* (3), 686–689.
- (31) Chorkendorff, I.; Rasmussen, P. B. Reconstruction of Cu(100) by Adsorption of Atomic Hydrogen. *Surf. Sci.* **1991**, *248* (1), 35–44.
- (32) Chang, X.; Li, J.; Xiong, H.; Zhang, H.; Xu, Y.; Xiao, H.; Lu, Q.; Xu, B. C–C Coupling Is Unlikely to Be the Rate-Determining Step in the Formation of  $\text{C}_2^+$  Products in the Copper-Catalyzed Electrochemical Reduction of CO. *Angew. Chem., Int. Ed.* **2022**, *61* (2), No. e202111167.
- (33) Cheng, D.; Wei, Z.; Zhang, Z.; Broekmann, P.; Alexandrova, A. N.; Sautet, P. Restructuring and Activation of Cu(111) under Electrocatalytic Reduction Conditions. *Angew. Chem., Int. Ed.* **2023**, *62* (20), No. e202218575.
- (34) Huynh, T. M. T.; Broekmann, P. From In Situ towards In Operando Conditions: Scanning Tunneling Microscopy Study of Hydrogen Intercalation in Cu(111) during Hydrogen Evolution. *ChemElectroChem* **2014**, *1* (8), 1271–1274.
- (35) Tackett, B. M.; Raciti, D.; Hight Walker, A. R.; Moffat, T. P. Surface Hydride Formation on Cu(111) and Its Decomposition to Form  $\text{H}_2$  in Acid Electrolytes. *J. Phys. Chem. Lett.* **2021**, *12*, 10936–10941.
- (36) Raciti, D.; Moffat, T. P. Quantification of Hydride Coverage on Cu(111) by Electrochemical Mass Spectrometry. *J. Phys. Chem. C* **2022**, *126* (44), 18734–18743.
- (37) Raciti, D.; Cockayne, E.; Vinson, J.; Schwarz, K.; Hight Walker, A. R.; Moffat, T. P. SHINERS Study of Chloride Order–Disorder Phase Transition and Solvation of Cu(100). *J. Am. Chem. Soc.* **2024**, *146* (2), 1588–1602.
- (38) Cheng, D.; Alexandrova, A. N.; Sautet, P. H-Induced Restructuring on Cu(111) Triggers  $\text{CO}$  Electroreduction in an Acidic Electrolyte. *J. Phys. Chem. Lett.* **2024**, *15* (4), 1056–1061.
- (39) Zhang, Z.; Gee, W.; Sautet, P.; Alexandrova, A. N. H and CO Co-Induced Roughening of Cu Surface in  $\text{CO}_2$  Electroreduction Conditions. *J. Am. Chem. Soc.* **2024**, *146* (23), 16119–16127.

(40) Friebel, D.; Mbuga, F.; Rajasekaran, S.; Miller, D. J.; Ogasawara, H.; Alonso-Mori, R.; Sokaras, D.; Nordlund, D.; Weng, T.-C.; Nilsson, A. Structure, Redox Chemistry, and Interfacial Alloy Formation in Monolayer and Multilayer Cu/Au(111) Model Catalysts for CO<sub>2</sub> Electroreduction. *J. Phys. Chem. C* **2014**, *118* (15), 7954–7961.

(41) Trimarco, D. B.; Scott, S. B.; Thilsted, A. H.; Pan, J. Y.; Pedersen, T.; Hansen, O.; Chorkendorff, I.; Vesborg, P. C. K. Enabling Real-Time Detection of Electrochemical Desorption Phenomena with Sub-Monolayer Sensitivity. *Electrochim. Acta* **2018**, *268*, 520–530.

(42) Trimarco, D. B.; Pedersen, T.; Hansen, O.; Chorkendorff, I.; Vesborg, P. C. K. Fast and Sensitive Method for Detecting Volatile Species in Liquids. *Rev. Sci. Instrum.* **2015**, *86* (7), No. 075006.

(43) Krempel, K.; Hochfilzer, D.; Scott, S. B.; Kibsgaard, J.; Vesborg, P. C. K.; Hansen, O.; Chorkendorff, I. Dynamic Interfacial Reaction Rates from Electrochemistry–Mass Spectrometry. *Anal. Chem.* **2021**, *93* (18), 7022–7028.

(44) Gründer, Y.; Drünkler, A.; Golks, F.; Wijts, G.; Stettner, J.; Zegenhagen, J.; Magnussen, O. M. Structure and Electrocompression of Chloride Adlayers on Cu(111). *Surf. Sci.* **2011**, *605* (17), 1732–1737.

(45) Moffat, T. P. STM Study of the Influence of Adsorption on Step Dynamics. *MRS Online Proc. Libr.* **1996**, *451* (1), 75–80.

(46) Vasiljevic, N.; Dimitrov, N.; Sieradzki, K. Pattern Organization on Cu(111) in Perchlorate Solutions. *J. Electroanal. Chem.* **2006**, *595* (1), 60–70.

(47) Friebel, D.; Mangen, T.; Obliers, B.; Schlaup, C.; Broekmann, P.; Wandelt, K. On the Existence of Ordered Organic Adlayers at the Cu(111)/Electrolyte Interface. *Langmuir* **2004**, *20* (7), 2803–2806.

(48) Tian, Y.; Hong, J.; Cao, D.; You, S.; Song, Y.; Cheng, B.; Wang, Z.; Guan, D.; Liu, X.; Zhao, Z.; Li, X.-Z.; Xu, L.-M.; Guo, J.; Chen, J.; Wang, E.-G.; Jiang, Y. Visualizing Eigen/Zundel Cations and Their Interconversion in Monolayer Water on Metal Surfaces. *Science* **2022**, *377* (6603), 315–319.

(49) Foresti, M. L.; Innocenti, M.; Forni, F.; Guidelli, R. Electro-sorption Valency and Partial Charge Transfer in Halide and Sulfide Adsorption on Ag(111). *Langmuir* **1998**, *14* (24), 7008–7016.

(50) Broekmann, P.; Wilms, M.; Kruff, M.; Stuhlmann, C.; Wandelt, K. In-Situ STM Investigation of Specific Anion Adsorption on Cu(111). *J. Electroanal. Chem.* **1999**, *467* (1), 307–324.

(51) Yang, H.; Dianat, A.; Bobeth, M.; Cuniberti, G. Modeling of the Co-adsorption of Chloride and Hydrogen Ions on Copper Electrode Surface. *J. Electrochem. Soc.* **2019**, *166* (1), D3042–D3048.

(52) Jiang, T.; Brisard, G. M. Determination of the Kinetic Parameters of Oxygen Reduction on Copper Using a Rotating Ring Single Crystal Disk Assembly (RRDCu(Hkl)E). *Electrochim. Acta* **2007**, *52* (13), 4487–4496.

(53) Brisard, G.; Bertrand, N.; Ross, P. N.; Marković, N. M. Oxygen Reduction and Hydrogen Evolution–Oxidation Reactions on Cu(Hkl) Surfaces. *J. Electroanal. Chem.* **2000**, *480* (1), 219–224.

(54) Kok, J.; de Ruiter, J.; van der Stam, W.; Burdyny, T. Interrogation of Oxidative Pulsed Methods for the Stabilization of Copper Electrodes for CO<sub>2</sub> Electrolysis. *J. Am. Chem. Soc.* **2024**, *146* (28), 19509–19520.



CAS BIOFINDER DISCOVERY PLATFORM™

## CAS BIOFINDER HELPS YOU FIND YOUR NEXT BREAKTHROUGH FASTER

Navigate pathways, targets, and  
diseases with precision

Explore CAS BioFinder

